

Optimal Transport Driven Asymmetric Image-to-Image Translation for Nuclei Segmentation of Histological Images

Suman Mahapatra and Pradipta Maji

Abstract—Segmentation of nuclei regions from histological images enables morphometric analysis of nuclei structures, which in turn helps in the detection and diagnosis of diseases under consideration. To develop a nuclei segmentation algorithm, applicable to different types of target domain representations, image-to-image translation networks can be considered as they are invariant to target domain image representations. One of the important issues with image-to-image translation models is that they fail miserably when the information content between two image domains are asymmetric in nature. In this regard, the paper introduces a new deep generative model for segmenting nuclei structures from histological images. The proposed model considers an embedding space for handling information-disparity between information-rich histological image space and information-poor segmentation map domain. Integrating judiciously the concepts of optimal transport and measure theory, the model develops an invertible generator, which provides an efficient optimization framework with lower network complexity. The concept of invertible generator automatically eliminates the need of any explicit cycle-consistency loss. The proposed model also introduces a spatially-constrained squeeze operation within the framework of invertible generator to maintain spatial continuity within the image patches. The model provides a better trade-off between network complexity and model performance compared to other existing models having complex network architectures. An important finding is that the proposed model performs significantly better than the state-of-the-art methods in 87.5% cases with respect to standard segmentation evaluation metrics, considering publicly available TCGA and CoNIC data sets. The performance of the proposed deep generative model, along with a comparison with state-of-the-art nuclei segmentation methods, is demonstrated on publicly available histological image data sets.

Index Terms—Image-to-image translation, deep learning, optimal transport, histological image analysis, nuclei segmentation.

I. INTRODUCTION

MICROSCOPIC analysis of histological tissue images plays a very crucial role in the diagnosis, prognosis and treatment of cancer due to the abundance of phenotypic information present in histological images [1]. With the advent of digital pathology, computer-aided analysis of tissue images has become an integral step in the field of medical image analysis as it can ease pathologists' tasks. The grades of different types of cancers are determined by analyzing different shapes and spatial arrangements of nuclei regions within a tissue specimen [2]. Hence, segmentation of nuclei structures from histological images has an immense importance in digital pathology as it provides significant morphological information, which helps in the therapeutic diagnosis of diseases under consideration.

Segmenting nuclei structures from histological images is a challenging task as nuclei can exhibit different morphologies, color, texture or can be occluded partially by other nuclei or different cellular components.

Nuclei segmentation is a process that focuses on the labeling of all pixels corresponding to each individual nucleus, and separating each nucleus from the background, other nuclei and different cellular components in a tissue image. Some earlier works in this domain have relied on energy-based methods, particularly the watershed algorithm. In [3], fast radial symmetry transform was employed to extract marker corresponding to each histological image and a sequence of different morphological operations was utilized to obtain the energy landscape. A variant of the watershed algorithm, which solely depends on the extracted energy landscape, was proposed in [4]. It uses a combination of active contour and shape prior to extract nuclei regions from histological images. In [5], a nuclei segmentation method was proposed, which utilizes the geometry of nuclei structures to compute the concavity of nuclei clusters. Based on the combination of double thresholding method and different morphological operations, a cell/nuclei segmentation approach was proposed in [6]. However, these methods are sensitive to the choice of pre-defined parameters and assume the shapes of the nuclei apriori, leading to the extraction of faulty segmentation maps since nuclei can exhibit diverse shapes across different organs. Some shallow learning based models [7], [8], which perform convolution operation directly on histological images, utilize their abstract feature representations to extract pixel-wise labels from each input histological image. The main concern with these shallow learning based approaches is that they do not consider spatial dependency between image pixels and eventually extract inaccurate nuclei segmentation maps.

Recent years have witnessed a huge surge in the application of deep learning based models in various medical image analysis tasks. In [9], Ronneberger *et al.* proposed U-Net model, which has been applied in numerous biomedical image segmentation tasks. The U-Net architecture incorporates the concept of skip connections in traditional encoder-decoder framework to capture low-level semantic information. The U-Net++ model [10], an extension of the U-Net architecture, enables feature propagation through densely interconnected skip connections. Another extension of the U-Net architecture was proposed in [11] for proper detection and segmentation of nuclei regions of different sizes. In a recent method [12], an attention mechanism based U-Net model has been introduced

for the segmentation of blood vessels from retinal images. However, U-Net based methods often fail to detect clustered nuclei and are extremely sensitive to pre-defined parameters associated with weighted loss function. A supervised two-stage object segmentation method, called Mask-R-CNN, was proposed in [13] for segmenting objects from natural as well as medical images. The Mask-R-CNN model predicts bounding boxes corresponding to each individual nucleus, and then, the nuclei regions are segmented inside the predicted bounding boxes. In [14], a unified fully convolutional network based model, named HoVer-Net, was proposed for simultaneous segmentation and classification of nuclei structures. This method utilizes the concepts of vertical and horizontal distance maps in order to separate occluded or touching nuclei structures. Most of these aforementioned approaches need a large number of annotated images, which are sometimes practically infeasible to have due to the time, effort and expert knowledge needed to annotate the data. A nuclei instance segmentation and classification approach, named Stardist, was proposed in [15]. Though Stardist performs well in case of convex object shapes, it fails miserably to detect heterogeneous nuclei shapes. This is due to the fact that Stardist assumes the nuclei shapes to be star-convex in nature, which is an impractical assumption about nuclei structures belonging to different organs of the body. Recently, Swin transformer, which is a type of vision transformer, has emerged as a new tool for image segmentation problems. In [16], a Swin transformer based dual encoder-decoder architecture has been proposed for polyp segmentation from colonoscopy images. A Swin transformer based multiple instance learning method, named Swin-MIL, has been proposed in [17] for predicting masks from histological images. The main disadvantage with the vision transformer based models is that they are computationally expensive due to the large number of parameters involved and also need a substantial number of samples for training the models. In a recent method, called BoNuS [18], a binary mining loss term has been introduced to simultaneously learn nuclei interior and extract boundary information in order to segment nuclei structures from histological images.

Image-to-image (I2I) translation models aim to learn mappings between image domains while preserving certain high-level semantic information. One important characteristic of the I2I models is that they are invariant to different types of target domain image representations, shapes and sizes of the objects, which enhance the applicability of the translation models. To achieve unpaired training between two image domains, CycleGAN model was proposed in [19], based on the concept of generative adversarial networks (GAN). Along with two generators: one for the forward mapping and the other one for inverse mapping corresponding to two image domains, CycleGAN model also introduced the concept of cycle-consistency loss term. In [20], conditional GAN with spectral normalization is employed in CycleGAN [19] framework for generating synthetic data and subsequently segmenting nuclei regions from histological images. A pathology-constrained CycleGAN model was proposed in [21] for stain transfer, which can be utilized to address the nuclei segmentation problem. However, the CycleGAN based models fail in accurate segmentation of

nuclei structures as the information content within the two image domains are asymmetric in nature. The histological images contain information regarding cell nuclei along with other tissue-level details, compared to segmentation maps, which contain information regarding only nuclei structures. Another concern with the CycleGAN based models is that they incorporate one generator and one discriminator corresponding to each of the image domains, which eventually increase the network complexity. In cycle-free CycleGAN model [22], the concept of optimal transport is utilized to achieve unpaired I2I translation with lower network complexity. But, cycle-free CycleGAN model does not consider information disparity between histological image domain and segmentation map space. As a result, the extracted nuclei segmentation maps are expected to be less accurate. Hence, an I2I translation model needs to be developed to solve the nuclei segmentation problem by handling the information disparity present among two asymmetric image domains.

In this respect, the paper introduces a new deep generative model, termed as Ostrich (Optimal Transport Driven Asymmetric Image-to-Image Translation approach), for segmentation of nuclei structures from histological images. Particularly, the paper makes the following contributions:

- The proposed Ostrich model is capable of handling information-asymmetry between information-rich histological image space and information-poor segmentation map domain by considering an embedding space to balance the information disparity between two asymmetric image domains.
- The proposed model combines the concept of optimal transport with measure theory to develop an invertible generator, which provides an efficient optimization framework with lower network complexity as well as eliminates the need of any explicit cycle-consistency loss term.
- The model also introduces a simple yet effective spatially-constrained squeeze operation within the framework of coupling layers associated with invertible generator to maintain intra-image spatial continuity.
- The proposed model provides a better trade-off between network complexity and model performance compared to other existing models having more complex network architectures.

The efficacy of the proposed Ostrich model, along with a comparison with state-of-the-art nuclei segmentation approaches, has been established on publicly available H&E stained histological image data sets.

II. OSTRICH: PROPOSED METHOD

In this section, a deep generative model, based on the theory of optimal transport [23], is presented for nuclei segmentation from histological images. The proposed model is inspired by the cycle-free CycleGAN model introduced in [22]. The main difference between the proposed Ostrich model and [22] is that the Ostrich model tries to perform image-to-image translation between two image domains with information imbalance, which the cycle-free CycleGAN model [22] is not capable of dealing with.

A. Problem Statement

Given a histological image domain \mathcal{X} , containing a set of n number of images $\{x_i : i = 1, 2, \dots, n\}$, the aim is to develop a model, which takes each histological image $x_i \in \mathcal{X} \subset \mathbb{R}^{H \times W \times 3}$ as input and outputs corresponding nuclei segmentation map y_i . The set of these output maps $\{y_i\}$ forms segmentation map domain \mathcal{Y} , that is, $y_i \in \mathcal{Y} \subset \mathbb{R}^{H \times W}$. As described in the previous section, there is an observable information-imbalance between the two image domains: histological image space \mathcal{X} and segmentation map domain \mathcal{Y} . Hence, the goal of the current study is to design a deep generative model that, with proper training, will be able to generate segmentation annotation map corresponding to each input histological image by handling the information-asymmetry between two image domains.

B. Cycle-free Asymmetric I2I Translation

This subsection introduces an invertible I2I translation approach for solving the problem of nuclei segmentation of histological images. The following analysis establishes that two generators and one discriminator are sufficient to solve this problem.

To balance the information-asymmetry while translating from information-rich image space \mathcal{X} to information-poor segmentation map domain \mathcal{Y} , an embedding space \mathcal{Z} is considered in this study. Let, the histological image space \mathcal{X} be equipped with probability measure μ , whereas the annotation image space \mathcal{Y} and the embedding space \mathcal{Z} be equipped with probability measures ν and η , respectively. The aim of the proposed model is to transport the joint distribution of ν and η of the annotation domain \mathcal{Y} and embedding space \mathcal{Z} , respectively, that is, $(\nu \times \eta)$, to distribution μ of the image space \mathcal{X} so that the joint distribution can mimic the distribution of the histological image space.

In the proposed model, three generators F_ϕ , E_ω , and G_θ are considered. The forward operator F_ϕ “pushes forward” measure μ in image space \mathcal{X} to measure ν_ϕ in the annotation space \mathcal{Y} , that is, $F_\phi : \mathcal{X} \rightarrow \mathcal{Y}$. Similarly, the transportation from probability space (\mathcal{X}, μ) to (\mathcal{Z}, η) is performed by the forward operator E_ω , which pushes forward measure μ in image space \mathcal{X} to η_ω in the embedding space \mathcal{Z} , that is, $E_\omega : \mathcal{X} \rightarrow \mathcal{Z}$. On the other hand, the generator G_θ transports the product measure $(\nu \times \eta)$ in the product space $(\mathcal{Y} \times \mathcal{Z})$ to μ_θ in the target histological image space \mathcal{X} , that is, $G_\theta : (\mathcal{Y} \times \mathcal{Z}) \rightarrow \mathcal{X}$. Hence, the optimal transport problem in this study can be solved by minimizing the distances $d(\mu, \mu_\theta)$, $d(\nu, \nu_\phi)$, and $d(\eta, \eta_\omega)$, where $d(\alpha, \beta)$ denotes statistical distance between two probability measures α and β . So, to solve this simultaneous statistical distance minimization problem, the following optimal transport problem needs to be solved:

$$\inf_{\pi \in \Pi(\mu, \nu, \eta)} \int_{\mathcal{X} \times \mathcal{Y} \times \mathcal{Z}} C(x, y, z; G_\theta, F_\phi, E_\omega) d\pi(x, y, z) \quad (1)$$

where $\Pi(\mu, \nu, \eta)$ denotes the set of all joint probability distributions with the marginals μ , ν , and η . In this study, the

transportation cost is defined as follows:

$$C(x, y, z; G_\theta, F_\phi, E_\omega) = \|x - G_\theta(y, z)\| + \|F_\phi(x) - y\| + \|E_\omega(x) - z\|. \quad (2)$$

At the initial stage, the output segmentation maps, generated by the forward operator F_ϕ , are far from the real data distribution in \mathcal{Y} . So, to push the generation in the proper direction, a regularization term is introduced in the current study, which is defined as follows:

$$l_{ssim}(F_\phi) = \|1 - SSIM(F_\phi(x), VO(f_{rgb}^{hed}(x)[:, :, 0]))\|. \quad (3)$$

Here, $SSIM$ denotes a structural similarity measurement index, called structural similarity index measure [24], $f_{rgb}^{hed}(\cdot)$ represents a function for converting a color image from RGB to Hematoxylin-Eosin-DAB (HED) colorspace. As nuclei regions in a H&E-stained image are generally highlighted by hematoxylin (H) stain, the H-channel of an image $x \in \mathcal{X}$ is considered through $f_{rgb}^{hed}(x)[:, :, 0]$. $VO(\cdot)$ denotes a transformation, which takes the H-channel image as input and outputs corresponding segmentation map by leveraging Voronoi labeling on thresholded H-channel image due to Otsu [25]. The aim is to maximize the structural similarity between the generated output and the transformed output through this regularization term. So, considering the regularization term, the overall transportation cost is defined as follows:

$$C(x, y, z; G_\theta, F_\phi, E_\omega) = \|x - G_\theta(y, z)\| + \|F_\phi(x) - y\| + \|E_\omega(x) - z\| + \lambda_1 l_{ssim}(F_\phi) \quad (4)$$

where λ_1 denotes the relative importance of the regularization term $l_{ssim}(F_\phi)$, defined in (3). The value of λ_1 decreases gradually during the training. The computation of the regularization term is trivial, but from the perspective of optimal transport, the computation of the first three terms requires corresponding dual formulation [23], [26].

The conversion from primal to dual form is provided in the appendix. The dual formulation corresponding to the optimal transport problem presented in (1), with the transportation cost $C(x, y, z; G_\theta, F_\phi, E_\omega)$, defined in (4), can be represented as follows:

$$\min_{\theta, \phi, \omega} \max_{\varphi, \psi, \xi} l(G_\theta, F_\phi, E_\omega; \varphi, \psi, \xi) \quad (5)$$

where φ , ψ and ξ represent three discriminators corresponding to three domains \mathcal{X} , \mathcal{Y} and \mathcal{Z} , respectively. Here, the loss $l(G_\theta, F_\phi, E_\omega; \varphi, \psi, \xi)$ is defined as follows:

$$l(G_\theta, F_\phi, E_\omega; \varphi, \psi, \xi) = l_{GAN}(G_\theta, F_\phi, E_\omega; \varphi, \psi, \xi) + \lambda_2 l_{cycle}(G_\theta, F_\phi, E_\omega) + \lambda_1 l_{ssim}(F_\phi) \quad (6)$$

where the optimal transport based GAN loss term

$l_{GAN}(G_\theta, F_\phi, E_\omega; \varphi, \psi, \xi)$ is defined as follows:

$$\begin{aligned}
& l_{GAN}(G_\theta, F_\phi, E_\omega; \varphi, \psi, \xi) = \\
& \max_{\varphi \in Lip_1(\mathcal{X})} \left[\int_{\mathcal{X}} \varphi(x) d\mu(x) - \int_{\mathcal{Y} \times \mathcal{Z}} \varphi(G_\theta(y, z)) d(\nu \times \eta)(y, z) \right] \\
& + \max_{\psi \in Lip_1(\mathcal{Y})} \left[\int_{\mathcal{Y}} \psi(y) d\nu(y) - \int_{\mathcal{X}} \psi(F_\phi(x)) d\mu(x) \right] \\
& + \max_{\xi \in Lip_1(\mathcal{Z})} \left[\int_{\mathcal{Z}} \xi(z) d\eta(z) - \int_{\mathcal{X}} \xi(E_\omega(x)) d\mu(x) \right] \quad (7)
\end{aligned}$$

where $Lip_m(D)$ represents the space of all m -Lipschitz functions defined over domain D . G_θ is a $(\nu \times \eta)$ -measurable function defined on the product space $(\mathcal{Y} \times \mathcal{Z})$. So, the sections of G_θ , that is, G_{θ_y} and G_{θ^z} , are η -measurable function defined on \mathcal{Z} space and ν -measurable function defined on domain \mathcal{Y} , respectively [27].

The parameter λ_2 in (6) denotes the relative importance of the cycle-consistency loss term $l_{cycle}(G_\theta, F_\phi, E_\omega)$, which can be defined as follows:

$$\begin{aligned}
l_{cycle}(G_\theta, F_\phi, E_\omega) &= \int_{\mathcal{X}} \|x - G_{\theta^z}(F_\phi(x))\| d\mu(x) \\
&+ \int_{\mathcal{X}} \|x - G_{\theta_y}(E_\omega(x))\| d\mu(x) + \int_{\mathcal{Y}} \|y - F_\phi(G_{\theta^z}(y))\| d\nu(y) \\
&+ \int_{\mathcal{Z}} \|z - E_\omega(G_{\theta_y}(z))\| d\eta(z) \quad (8)
\end{aligned}$$

Theorem 1: If the sections of generator G_θ , that is, G_{θ_y} and G_{θ^z} , are considered to be the inverse operators of forward operators E_ω and F_ϕ , respectively, that is, $G_{\theta_y} = E_\omega^{-1}$ and $G_{\theta^z} = F_\phi^{-1}$ and G_{θ^z} is a p -Lipschitz function in domain \mathcal{Y} , then the problem in (5) with $p = 1$, can be represented by the following equivalent problem:

$$\min_{\phi, \omega} \max_{\psi, \xi} l(F_\phi, E_\omega; \psi, \xi) \quad (9)$$

$$\begin{aligned}
\text{where } l(F_\phi, E_\omega; \psi, \xi) &= 2l_{GAN}(F_\phi; \psi) \\
&+ l_{GAN}(E_\omega; \xi) + \lambda_1 l_{sim}(F_\phi) \quad (10)
\end{aligned}$$

and

$$l_{GAN}(F_\phi; \psi) = \max_{\psi \in Lip_1(\mathcal{Y})} \left[\int_{\mathcal{Y}} \psi(y) d\nu(y) - \int_{\mathcal{X}} \psi(F_\phi(x)) d\mu(x) \right] \quad (11)$$

$$l_{GAN}(E_\omega; \xi) = \max_{\xi \in Lip_1(\mathcal{Z})} \left[\int_{\mathcal{Z}} \xi(z) d\eta(z) - \int_{\mathcal{X}} \xi(E_\omega(x)) d\mu(x) \right] \quad (12)$$

Proof. The invertibility conditions $G_{\theta_y} = E_\omega^{-1}$ and $G_{\theta^z} = F_\phi^{-1}$ ensure that $G_{\theta_y}(E_\omega(x)) = x$, $G_{\theta^z}(F_\phi(x)) = x$, $F_\phi(G_{\theta^z}(y)) = y$ and $E_\omega(G_{\theta_y}(z)) = z$. So, it is evident that if the above invertibility conditions hold, then the cycle-consistency loss term $l_{cycle}(G_\theta, F_\phi, E_\omega)$ vanishes.

Let, $\varphi^* \in Lip_1(\mathcal{X})$ be the optimum 1-Lipschitz function in domain \mathcal{X} for which the first sub-expression from (7) attains maximum value. So,

$$\begin{aligned}
& \max_{\varphi \in Lip_1(\mathcal{X})} \left[\int_{\mathcal{X}} \varphi(x) d\mu(x) - \int_{\mathcal{Y} \times \mathcal{Z}} \varphi(G_\theta(y, z)) d(\nu \times \eta)(y, z) \right] \\
&= \int_{\mathcal{X}} \varphi^*(x) d\mu(x) - \int_{\mathcal{Y} \times \mathcal{Z}} \varphi^*(G_\theta(y, z)) d(\nu \times \eta)(y, z). \quad (13)
\end{aligned}$$

Let, the two terms in (13) be denoted by J_1 and J_2 , respectively, that is,

$$J_1 = \int_{\mathcal{X}} \varphi^*(x) d\mu(x) \quad (14)$$

$$\text{and } J_2 = - \int_{\mathcal{Y} \times \mathcal{Z}} \varphi^*(G_\theta(y, z)) d(\nu \times \eta)(y, z). \quad (15)$$

As G_{θ^z} is designed to be the inverse of forward operator F_ϕ , the following formulation can be derived from (14):

$$J_1 = \int_{\mathcal{X}} \varphi^*(G_{\theta^z}(F_\phi(x))) d\mu(x) = \max_{\psi \in \Phi_1} \int_{\mathcal{X}} \psi_\theta(F_\phi(x)) d\mu(x) \quad (16)$$

where the set Φ_1 is defined as follows:

$$\Phi_1 = \{\hat{\psi} | \hat{\psi} = \varphi \circ G_{\theta^z}, \varphi \in Lip_1(\mathcal{X}), G_{\theta^z} \in Lip_1(\mathcal{Y})\}. \quad (17)$$

Here, ‘ \circ ’ denotes the composition of functions. Now, (15) can be rewritten as follows:

$$J_2 = \max_{\mathcal{H}_\theta \in \Phi_2} \left[- \int_{\mathcal{Y} \times \mathcal{Z}} \mathcal{H}_\theta(y, z) d(\nu \times \eta)(y, z) \right]. \quad (18)$$

Here, the set Φ_2 is defined as follows:

$$\Phi_2 = \{\mathcal{H} | \mathcal{H} = \varphi \circ G_\theta, \varphi \in Lip_1(\mathcal{X})\}. \quad (19)$$

Using Fubini’s theorem on product measures [27], (18) can be formulated as follows:

$$J_2 = \max_{\mathcal{H}_\theta \in \Phi_2} \left[- \int_{\mathcal{Y}} \left\{ \int_{\mathcal{Z}} \mathcal{H}_\theta(y, z) d\eta(z) \right\} d\nu(y) \right]. \quad (20)$$

The expression $\int_{\mathcal{Z}} \mathcal{H}_\theta(y, z) d\eta(z)$ in (20) is a ν -measurable function and is defined on space \mathcal{Y} . Let, the expression be

denoted by $\mathcal{M}_\theta(y)$. For any two points $y_1, y_2 \in \mathcal{Y}$,

$$\begin{aligned}
& \|\mathcal{M}_\theta(y_1) - \mathcal{M}_\theta(y_2)\| \\
&= \left\| \int_{\mathcal{Z}} \mathcal{H}_\theta(y_1, z) d\eta(z) - \int_{\mathcal{Z}} \mathcal{H}_\theta(y_2, z) d\eta(z) \right\| \\
&\leq \int_{\mathcal{Z}} \|\mathcal{H}_\theta(y_1, z) - \mathcal{H}_\theta(y_2, z)\| d\eta(z) \\
&\leq \int_{\mathcal{Z}} \|G_\theta(y_1, z) - G_\theta(y_2, z)\| d\eta(z) \\
&\quad [\text{as } \mathcal{H}_\theta = \varphi \circ G_\theta \text{ and } \varphi \in Lip_1(\mathcal{X})] \\
&= \int_{\mathcal{Z}} \|G_\theta^z(y_1) - G_\theta^z(y_2)\| d\eta(z) \leq \|y_1 - y_2\| \int_{\mathcal{Z}} d\eta(z) \\
&= \|y_1 - y_2\| \quad [\text{as } G_\theta^z \in Lip_1(\mathcal{Y})]. \tag{21}
\end{aligned}$$

Thus, (20) can be reformulated as follows:

$$J_2 = \max_{\mathcal{M}_\theta \in \Phi_3} \left[- \int_{\mathcal{Y}} \mathcal{M}_\theta(y) d\nu(y) \right] \tag{22}$$

where the set Φ_3 can be defined as follows:

$$\Phi_3 = \{ \mathcal{M} | \mathcal{M} = \int_{\mathcal{Z}} \mathcal{H}(y, z) d\eta(z), \mathcal{H} \in \Phi_2 \}. \tag{23}$$

Hence, the set Φ_3 constructs a subset of the set of all 1-Lipschitz functions on domain \mathcal{Y} . Again, for any element $\hat{\psi}_1 \in \Phi_1$, $\hat{\psi}_1$ is of the form $\hat{\psi}_1 = \varphi_1 \circ g$, where $\varphi_1 \in Lip_1(\mathcal{X})$ and $g \in Lip_1(\mathcal{Y})$. So, g can potentially be any element from the set Φ_3 and $\hat{\psi}_1$ can map the element to $Lip_1(\mathcal{Y})$ within or beyond Φ_3 . So, the above argument ensures that Φ_3 is contained in Φ_1 , that is, $\Phi_3 \subseteq \Phi_1$. Hence, by combining (16) and (22), the following relation can be deduced:

$$\begin{aligned}
J_1 + J_2 &\leq \max_{\psi' \in \Phi_1} \left[\int_{\mathcal{X}} \psi'(F_\phi(x)) d\mu(x) - \int_{\mathcal{Y}} \psi'(y) d\nu(y) \right] \\
&= \max_{\psi \in \Phi_1} \left[\int_{\mathcal{Y}} \tilde{\psi}(y) d\nu(y) - \int_{\mathcal{X}} \tilde{\psi}(F_\phi(x)) d\mu(x) \right]
\end{aligned}$$

[equality comes from the fact: $\tilde{\psi} = -\psi'$ and thus $\tilde{\psi} \in \Phi_1$]. (24)

Now, by extending the function space from set Φ_1 to $Lip_1(\mathcal{Y})$, the following relation can be obtained from (13) and (24):

$$\begin{aligned}
& \max_{\varphi \in Lip_1(\mathcal{X})} \left[\int_{\mathcal{X}} \varphi(x) d\mu(x) - \int_{\mathcal{Y} \times \mathcal{Z}} \varphi(G_\theta(y, z)) d(\nu \times \eta)(y, z) \right] \\
&\leq \max_{\psi \in Lip_1(\mathcal{Y})} \left[\int_{\mathcal{Y}} \psi(y) d\nu(y) - \int_{\mathcal{X}} \psi(F_\phi(x)) d\mu(x) \right]. \tag{25}
\end{aligned}$$

Next, it must be shown that the upper bound in (25) is tight. Let, ψ^* be the maximizer for (25). To show the tightness of the upper bound, it is important to show that there exists $\varphi \in Lip_1(\mathcal{X})$ such that, for $z \in \mathcal{Z}$:

$$\psi^*(y) = \varphi(G_\theta^z(y)) = \varphi(G_\theta(y, z)), \quad \forall y \in \mathcal{Y}.$$

Due to the invertibility condition $G_\theta^z = F_\phi^{-1}$, an element $x \in \mathcal{X}$ can always be found such that $x = F_\phi^{-1}(y) = G_\theta^z(y)$ for all $y \in \mathcal{Y}$. So,

$$\varphi(x) = \varphi(F_\phi^{-1}(F_\phi(x))) = \varphi(G_\theta^z(F_\phi(x))) = \psi^*(F_\phi(x)),$$

which achieves the above upper bound. Hence, the following interesting relation can be obtained from (25):

$$\begin{aligned}
& \max_{\varphi \in Lip_1(\mathcal{X})} \left[\int_{\mathcal{X}} \varphi(x) d\mu(x) - \int_{\mathcal{Y} \times \mathcal{Z}} \varphi(G_\theta(y, z)) d(\nu \times \eta)(y, z) \right] \\
&= \max_{\psi \in Lip_1(\mathcal{Y})} \left[\int_{\mathcal{Y}} \psi(y) d\nu(y) - \int_{\mathcal{X}} \psi(F_\phi(x)) d\mu(x) \right]. \tag{26}
\end{aligned}$$

Substituting (26) in (7), following relation can be deduced:

$$\begin{aligned}
& l_{GAN}(G_\theta, F_\phi, E_\omega; \varphi, \psi, \xi) \\
&= \frac{1}{3} \{ 2l_{GAN}(F_\phi; \psi) + l_{GAN}(E_\omega; \xi) \} \tag{27}
\end{aligned}$$

which proves the claim of *Theorem 1*.

The above analysis eliminates the need of additional discriminator φ and generator G_θ if $G_{\theta y}$ and G_θ^z are considered to be the inverse operators of forward operators E_ω and F_ϕ , respectively. From the optimization perspective, if the normalizing constants in (27) are not taken into consideration, then the model requires two generators F_ϕ and E_ω , and two discriminators ψ and ξ . As the discriminators ψ and ξ discriminate between real and fake/generated \mathcal{Y} domain data, and real and generated \mathcal{Z} space data, respectively, instead of two discriminators, one discriminator ψ_ξ is sufficient, which takes inputs in the form of pairs (y, z) . The discriminator $\psi_\xi(y, z)$ discriminates between the real pair (y, z) , where $y \sim \mathcal{Y}$ and $z \sim \mathcal{Z}$, and the generated/fake pair (y, z) , where $y \sim P_{F_\phi}(y | x)$ and $z \sim P_{E_\omega}(z | x)$ corresponding to the outputs generated through F_ϕ and E_ω , respectively. As a histological image x can be generated through the invertible generator G_θ^z for a given embedding information $z \in \mathcal{Z}$, corresponding to a segmentation map $y \in \mathcal{Y}$, G_θ^z can also be used for generating synthetic data during model training.

C. Model Structure

Fig. 1 presents the block diagram of the proposed deep generative model for nuclei segmentation from histological images. The forward operator F_ϕ generates segmentation map corresponding to each input histological image and generator E_ω embeds additional information while translating from information-rich image space \mathcal{X} to information-poor segmentation map domain \mathcal{Y} . The discriminator ψ_ξ discriminates between real and generated/fake pairs of segmentation map and embedding information. Each training image patch $x \in \mathcal{X}$ is fed into both forward operators $F_\phi(x; \Theta_\phi)$ and $E_\omega(x; \Theta_\omega)$, which output corresponding segmentation map y and embedding information z , respectively. Without loss of generality, \mathcal{Z} is assumed to follow standard normal distribution. Here, Θ_ϕ , Θ_ω and Θ_{ψ_ξ} denote the network parameters associated with the networks F_ϕ , E_ω and ψ_ξ , respectively. As G_θ^z is

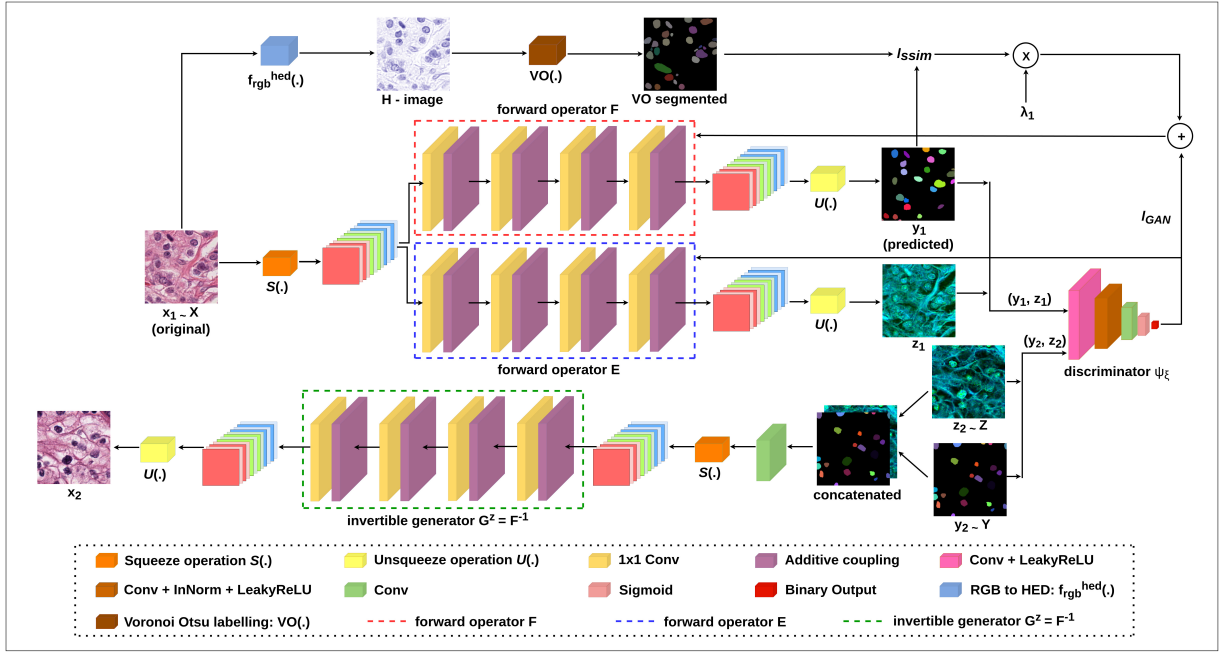


Fig. 1. Block diagram of the proposed deep generative model for nuclei segmentation of histological images. Each network component is marked with distinct color representation. In the diagram, 'Conv' means convolutional layer, ' 1×1 Conv' refers to invertible 1×1 convolution approach proposed in [28]. Given $z_2 \in \mathcal{Z}$, z_2 is concatenated with y_2 , and the concatenated image is fed to a convolution layer to produce a 3 channel output. 'InNorm' represents instance normalization, 'LeakyReLU' denotes leaky rectified linear unit. Here, forward operators F , E and invertible generator G^z refer to generators F_ϕ , E_ω and G_{θ^z} , respectively.

designed to be the inverse of the forward operator F_ϕ , G_{θ^z} uses the same parameter set Θ_ϕ as that of F_ϕ .

The overall objective of the proposed model is to generate segmentation map corresponding to each input histological image by handling the information-asymmetry between the two domains. The following min-max objective function J_{adv} is to be optimized to achieve the aforementioned objective:

$$J_{adv} = J(\psi_\xi) + J(F_\phi, E_\omega) \quad (28)$$

where $J(\psi_\xi)$ is the maximization objective, attributed by the discriminator ψ_ξ , and is given by

$$J(\psi_\xi) = \max_{\psi_\xi} \{l_{GAN}(F_\phi, E_\omega; \psi_\xi)\} \quad (29)$$

and $J(F_\phi, E_\omega)$ is the minimization objective, attributed by the two generators F_ϕ and E_ω , which is given by

$$\begin{aligned} J(F_\phi, E_\omega) &= \min_{\phi, \omega} \{l_{GAN}(F_\phi, E_\omega; \psi_\xi) + \lambda_1 l_{sim}(F_\phi)\} \\ &= \min_{\phi} \{l_{GAN}(F_\phi, E_\omega; \psi_\xi) + \lambda_1 l_{sim}(F_\phi)\} \\ &\quad + \min_{\omega} \{l_{GAN}(F_\phi, E_\omega; \psi_\xi)\} \end{aligned} \quad (30)$$

where $l_{GAN}(F_\phi, E_\omega; \psi_\xi)$ can be defined as follows:

$$\begin{aligned} l_{GAN}(F_\phi, E_\omega; \psi_\xi) &= \max_{\psi_\xi} \left[\int_{\mathcal{Y} \times \mathcal{Z}} \psi_\xi(y, z) d(\nu \times \eta)(y, z) \right. \\ &\quad \left. - \int_{\mathcal{X}} \psi_\xi(F_\phi(x), E_\omega(x)) d\mu(x) \right]. \end{aligned} \quad (31)$$

The main building block of the invertible generator is implemented using the concepts of invertible 1×1 convolution, proposed in [28] and general coupling layer, introduced in

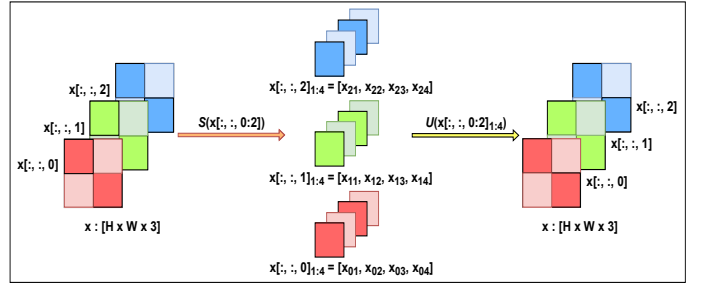


Fig. 2. Block diagram of the squeeze-unsqueeze operation. Here, $x[:, :, 0:2]$ denotes 3 channel input image. $x[:, :, i]_{1:4}$ represents 4 sub-patches of the i -th channel of input image $x \in \mathcal{X}$.

[29]. Algorithm 1 summarizes the training procedure for the proposed Ostrich model. To maintain the spatial continuity within the image patches, instead of checkerboard masking based squeeze operation explained in [22], a simple yet effective modified squeeze-unsqueeze operation is introduced in this study. For an input image $x \in \mathcal{X}$, the squeeze operation can be mathematically represented as follows:

$$[x[:, :, 0]_{1:4}, x[:, :, 1]_{1:4}, x[:, :, 2]_{1:4}] = S(x[:, :, 0:2]) = S(x)$$

whereas the unsqueeze operation can be defined as follows:

$$x = U([x[:, :, 0]_{1:4}]).$$

The squeeze operation $S(\cdot)$ and unsqueeze operation $U(\cdot)$ are demonstrated schematically through Fig. 2.

III. PERFORMANCE ANALYSIS

This section analyzes the performance of the proposed deep generative model, termed as Ostrich.

Algorithm 1 Mini-batch stochastic gradient descent training of proposed Ostrich model.

Input: A set of training images sampled from real data distribution $P_X(x)$, segmentation map images sampled from real data distribution $P_Y(y)$, number of training epochs (τ).

Output: Trained parameter set $\{\Theta_{\psi_\xi}, \Theta_{F_\phi}, \Theta_{E_\omega}\}$, corresponding to three deep neural networks ψ_ξ , F_ϕ and E_ω , respectively.

1: **for** each epoch $t = 0$ to $\tau - 1$ **do**

- Sample mini-batch of M images $\{x_m\}_{m=1}^M$ from real data distribution $P_X(x)$.
- Generate M nuclei segmentation maps $\{y_m\}_{m=1}^M$ by using $F_\phi(x_m; \Theta_\phi)$.
- Generate M embedding information maps $\{z_m\}_{m=1}^M$ by using $E_\omega(x_m; \Theta_\omega)$.
- Sample mini-batch of M nuclei segmentation maps $\{\hat{y}_m\}_{m=1}^M$ from real segmentation map image distribution $P_Y(y)$.
- Sample mini-batch of M embedding information maps $\{\hat{z}_m\}_{m=1}^M$ from embedding information prior $P_Z(z)$.
- Update discriminator ψ_ξ by ascending in the direction of stochastic gradient:

$$\nabla_{\Theta_{\psi_\xi}} \left(\frac{1}{M} \sum_{m=1}^M [\psi_\xi(\hat{y}_m, \hat{z}_m; \Theta_{\psi_\xi}) - \psi_\xi(y_m, z_m; \Theta_{\psi_\xi})] \right)$$

- Update segmentation map generator F_ϕ by descending in the direction of stochastic gradient:

$$\nabla_{\Theta_{F_\phi}} \left(\frac{1}{M} \sum_{m=1}^M [-\psi_\xi(y_m, z_m; \Theta_{\psi_\xi}) + \lambda_1 \|1 - SSIM(y_m, VO(f_{rgb}^{hed}(x_m)[:, :, 0]))\|] \right)$$

- Update embedding map generator E_ω by descending in the direction of stochastic gradient:

$$\nabla_{\Theta_{E_\omega}} \left(\frac{1}{M} \sum_{m=1}^M [-\psi_\xi(y_m, z_m; \Theta_{\psi_\xi})] \right)$$

2: **Stop**.

A. Experimental Setup

A brief description of the existing algorithms compared, data sets and quantitative indices used, and details regarding model training are provided next.

1) *Algorithms Compared*: The performance of the proposed Ostrich model in nuclei segmentation is analyzed extensively and compared with that of several standard object segmentation models, such as U-Net (2015) [9], Mask-RCNN (2017) [13], U-Net++ (2018) [10]; and state-of-the-art nuclei segmentation methods, namely, HoVer-Net (2019) [14], multi-organ nuclei segmentation (MoNS) (2020) [20], Stardist (2022) [15], Swin-MIL (2022) [17] and BoNuS (2024) [18].

2) *Data Sets Used*: The performance of different variants of the proposed model and several state-of-the-art algorithms in nuclei segmentation is analyzed using the following two publicly available data sets.

- TCGA Data [30]: This multi-organ image data set contains 30 images of resolution 1000×1000 , that were cropped from nuclei-dense regions of whole slide images downloaded from The Cancer Genome Atlas (TCGA). This H&E stained data set contains both instance segmentation and binary semantic segmentation maps corresponding to each histological image.
- CoNIC Data [31]: This H&E stained image set was published as a challenge data set: Colon Nuclei Identification and Counting (CoNIC) Challenge, 2022. The data set consists of 4,981 image patches having resolution of 256×256 . This data set contains instance segmentation maps corresponding to each histological image.

Four standard segmentation evaluation metrics, namely,

Dice coefficient, Jaccard index, precision and recall, are used to analyze the performance of different algorithms.

3) *Training Details*: The TCGA data set is randomly split into training, validation and test set with a ratio of 5 : 1 : 4. Hence, 2,535 overlapping image patches of size 256×256 corresponding to 15 training set images of TCGA data set have been used for training, whereas the validation set contains 507 overlapping patches and the test set comprises of 192 non-overlapping image patches corresponding to 3 and 12 images, respectively. The CoNIC data set consists of 4,981 image patches, among which 2,930 image patches have been used for training, 586 patches for validation and 1,465 images have been used for testing the performance of the proposed model. The incorporation of validation set for both the data sets prevents the model from over-fitting and ensures early stopping based on validation loss.

B. Performance Analysis on TCGA Data

The effectiveness of the proposed Ostrich model is validated through the following analyses.

1) *Ablation Study*: The objective function of the proposed Ostrich model is comprised of two constituent terms: a GAN objective term and a regularization term. Let, the regularization term $l_{ssim}(F_\phi)$ be denoted by R . The importance of the regularization term R is analyzed by an ablation study, where R is omitted from the objective function by setting $\lambda_1 = 0$. The performance of the proposed Ostrich model in nuclei segmentation is then compared with that of the model in the absence of R , and the corresponding results are presented in Table I. When λ_1 is set to 0, the model is referred to as

“Ostrich\(R ””. From the results reported in Table I, it is evident that the proposed model performs better than the “Ostrich\(R ” model with respect to all the segmentation evaluation indices used in this study. The qualitative comparison presented in Fig. 3 ensures that, with the initial perturbation through regularization term R , the proposed model is able to capture the intrinsic details of underlying data distribution. The statistical significance of the proposed Ostrich model is analyzed with respect to p-values computed through paired- t (one-tailed) and Wilcoxon signed-rank (one-tailed) tests. From the p-values reported in Table II, it can be observed that the proposed model performs significantly better than the “Ostrich\(R ” model, considering 95% confidence level, with respect to both paired- t and Wilcoxon signed-rank tests.

TABLE I
QUANTITATIVE PERFORMANCE ANALYSIS IN NUCLEI SEGMENTATION ON TCGA DATA SET: STATE-OF-THE-ART MODELS VS OSTRICH

Methods	Dice	Jaccard	Precision	Recall
Ostrich	0.788035	0.641520	0.813523	0.764096
Ostrich\(R	0.761814	0.606573	0.791683	0.734116
CycleGAN	0.754221	0.598782	0.764761	0.743967
OT-CycleGAN	0.766668	0.614903	0.804106	0.732561
Asym-CycleGAN	0.783812	0.638815	0.806971	0.761945
Checkerboard	0.772020	0.629522	0.785028	0.759437
U-Net (2015)	0.645650	0.446128	0.624558	0.668216
Mask-R-CNN (2017)	0.747086	0.585659	0.799975	0.700757
U-Net++ (2018)	0.773155	0.620294	0.796708	0.750955
HoVer-Net (2019)	0.744516	0.586780	0.811804	0.687529
MoNS (2020)	0.755509	0.614706	0.748012	0.763157
Stardist (2022)	0.743228	0.585713	0.811579	0.685495
Swin-MIL (2022)	0.749044	0.593266	0.801989	0.702656
BoNuS (2024)	0.784740	0.639496	0.806351	0.764257

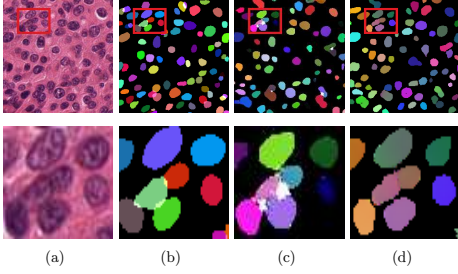


Fig. 3. Qualitative performance analysis in nuclei instance segmentation: (a) Original image, (b) Ground-truth; Segmentation performance of (c) Ostrich\(R and (d) Ostrich. Top row presents marked-up images from TCGA data, and bottom row presents the zoomed-in region from the marked-up patches.

2) *Comparison with Baseline Models*: The performance of the proposed Ostrich model is compared with that of two existing I2I translation models, namely, CycleGAN [19] and cycle-free CycleGAN [22]. To establish the significance of the proposed optimal transport and measure theory based analysis, the existing CycleGAN model is also extended by considering an embedding space for capturing additional information while translating from information-rich histological image space to information-poor segmentation map domain. This asymmetric CycleGAN model is comprised of three generators and three discriminators and is referred to as Asym-CycleGAN in this section. For simplicity, the optimal transport driven cycle-free CycleGAN model is referred to as OT-CycleGAN. Similar to

TABLE II
STATISTICAL SIGNIFICANCE ANALYSIS OF DIFFERENT ALGORITHMS WITH RESPECT TO PAIRED- t (ONE-TAILED) AND WILCOXON SIGNED RANK (ONE-TAILED) TESTS ON TCGA DATA SET

Methods	Test	Dice	Jaccard	Precision	Recall
Ostrich\(R		9.88E-30	3.41E-30	1.44E-09	1.30E-10
CycleGAN		4.88E-32	3.39E-34	3.69E-32	8.40E-10
OT-CycleGAN		2.90E-33	2.26E-33	1.04E-05	6.73E-21
Asym-CycleGAN		6.49E-02	5.42E-02	5.43E-05	8.31E-02
Checkerboard		4.66E-13	5.70E-14	1.83E-61	1.10E-02
U-Net (2015)	Paired- t	6.67E-30	4.18E-36	1.25E-76	6.68E-06
Mask-R-CNN (2017)		1.17E-37	4.55E-39	3.77E-05	1.28E-25
U-Net++ (2018)		1.08E-17	3.86E-18	5.03E-09	7.46E-03
HoVer-Net (2019)		1.77E-41	7.41E-45	2.37E-01	7.65E-54
MoNS (2020)		1.10E-14	1.84E-15	3.34E-48	1.21E-01
Stardist (2022)		1.46E-24	8.26E-26	3.09E-01	9.93E-27
Swin-MIL (2022)		1.95E-37	1.64E-41	1.74E-04	3.25E-49
BoNuS (2022)		1.42E-01	1.05E-01	9.20E-07	9.43E-01
Ostrich\(R	Wilcoxon	2.37E-23	2.34E-23	5.57E-07	2.01E-09
CycleGAN		9.05E-27	6.08E-27	1.66E-30	7.70E-10
OT-CycleGAN		8.58E-25	6.83E-25	7.49E-04	6.37E-18
Asym-CycleGAN		8.56E-02	7.80E-02	1.13E-03	7.67E-02
Checkerboard		7.74E-13	2.49E-13	8.57E-33	1.21E-02
U-Net (2015)		8.61E-32	7.06E-32	1.89E-33	4.45E-02
Mask-R-CNN (2017)		2.74E-28	3.20E-28	1.55E-03	1.41E-20
U-Net++ (2018)		9.70E-17	6.71E-17	2.86E-07	1.88E-03
HoVer-Net (2019)		1.63E-30	1.23E-30	6.85E-02	4.13E-32
MoNS (2020)		1.46E-13	3.65E-14	2.11E-33	1.10E-01
Stardist (2022)		7.73E-22	6.91E-22	3.40E-01	3.03E-23
Swin-MIL (2022)		9.15E-32	8.48E-32	3.83E-02	1.47E-32
BoNuS (2024)		8.18E-02	5.86E-02	7.36E-06	9.00E-01

TABLE III
NUMBER OF PARAMETERS INVOLVED IN EACH OF THE BASELINE I2I TRANSLATION MODELS AND OSTRICH (IN MILLIONS)

Methods	No. of Parameters (M)
CycleGAN	18.035
OT-CycleGAN	4.353
Asym-CycleGAN	27.053
Ostrich	7.271

the proposed Ostrich model, the regularization term $l_{sim}(F_\phi)$ is also incorporated in all three models, CycleGAN, OT-CycleGAN and Asym-CycleGAN for this comparative analysis. From the results reported in Table I, it can be observed that the proposed Ostrich model outperforms baseline I2I translation models, with respect to all the segmentation evaluation indices, namely, Dice, Jaccard, precision and recall. From the p-values reported in Table II, it can be noted that the Ostrich model performs significantly better than CycleGAN and OT-CycleGAN, and better than Asym-CycleGAN model, but not significantly. It is also evident from Table III that the proposed Ostrich model uses less number of parameters compared to CycleGAN and Asym-CycleGAN models. Though OT-CycleGAN uses less number of parameters than the proposed Ostrich model, it does not capture additional information to balance information asymmetry between two image domains, and eventually fails to outperform the proposed model. Through the qualitative representation presented in Fig. 4, it can also be observed that the proposed model performs better than all the aforementioned baseline models.

3) *Importance of Spatially-Constrained Squeeze Operation*: The performance of the proposed Ostrich model with spatially-constrained squeeze operation is compared with that of the

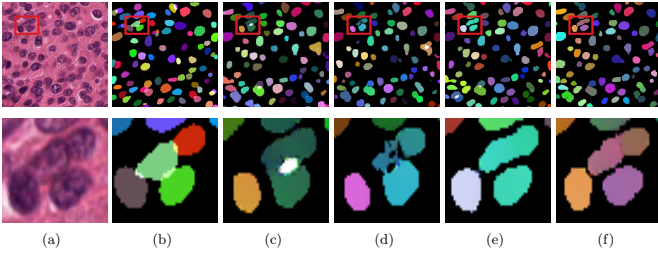


Fig. 4. Performance analysis in nuclei segmentation: (a) Original histological image, (b) Ground-truth segmentation map; segmentation performance of (c) CycleGAN, (d) OT-CycleGAN, (e) Asym-CycleGAN and (f) Ostrich. Top row presents marked-up images from TCGA data, and bottom row presents the zoomed-in region from the marked-up image patches.

proposed model with checkerboard masking based squeeze operation [22], and the corresponding results are reported in Table I. The values reported in Table I ensure the fact that spatially-constrained squeeze operation based proposed Ostrich model outperforms the model with checkerboard masking based squeeze operation, with respect to all the segmentation evaluation indices. The qualitative comparison of the performance of the proposed model and checkerboard masking based model is presented in Fig. 5. It can be observed in Fig. 5 that the proposed Ostrich model performs better than the checkerboard masking based model in separating overlapping nuclei structures. This is due to the fact that the proposed model can capture spatial connectivity through spatially-constrained squeeze operation, which checkerboard masking based model fails to capture. The p-values reported in Table II establish the fact that the proposed Ostrich model with spatially-constrained squeeze operation performs significantly better than the checkerboard masking based counterpart.

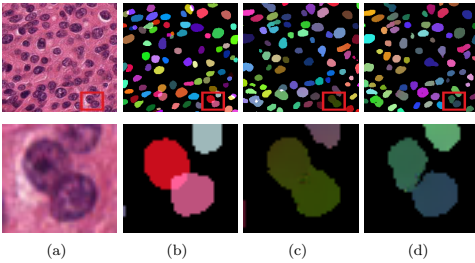


Fig. 5. Performance analysis of nuclei segmentation: (a) Original histological image, (b) Ground-truth; segmentation performance of models with (c) checkerboard masking based and (d) spatially-constrained squeeze operation. Top row presents marked-up images from TCGA data, and bottom row presents the zoomed-in region from the marked-up image patches.

4) *Performance in Binary Semantic Segmentation:* The performance of the proposed Ostrich model on TCGA data set in binary semantic segmentation is validated through the qualitative results presented in Fig. 6. It presents two image patches, their corresponding ground-truth images and two binary segmentation maps predicted by the proposed Ostrich model. From the qualitative analysis, it is clear that the proposed model can capture heterogeneous nuclei shapes. It is possible due to the fact that the proposed model does not assume the shapes of the nuclei objects apriori. The results reported in Table IV also ensure the fact that the proposed

Ostrich model performs well in binary semantic segmentation.

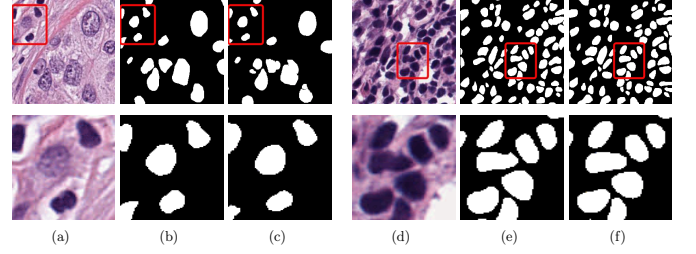


Fig. 6. Performance analysis in binary semantic segmentation: (a) histological image patch 1, (b) ground-truth segmentation map 1, (c) predicted map 1; (d) image patch 2, (e) ground-truth segmentation 2 and (f) predicted map 2. Top row presents marked-up images from TCGA data, and bottom row presents the zoomed-in region from the marked-up image patches.

TABLE IV
PERFORMANCE IN BINARY SEMANTIC SEGMENTATION

Model	Dice	Jaccard	Precision	Recall
Ostrich	0.810099	0.746830	0.817761	0.802580

5) *Comparison with State-of-the-Art Methods:* The performance of the proposed Ostrich model is finally compared with that of several state-of-the-art nuclei segmentation approaches on TCGA data set and the results with respect to different quantitative indices are reported in Table I. From the results reported in Table I, it can be observed that, in case of TCGA data, the proposed model outperforms all the state-of-the-art nuclei segmentation approaches, with respect to three segmentation evaluation indices, namely, Dice, Jaccard and precision. With respect to recall score, BoNuS performs slightly better than the proposed Ostrich model. The qualitative performance of the Ostrich model, along with a comparison with state-of-the-art approaches, in nuclei segmentation, is presented in Fig. 7 using two image patches from the TCGA data set. Analyzing the p-values reported in Table II, it is evident that, with respect to both paired-*t* and Wilcoxon signed-rank tests, the proposed Ostrich model performs significantly better in 29 out of 36 cases, better but not significantly in 6 cases.

C. Performance Analysis on CoNIC Data

Finally, the performance of the proposed Ostrich model is compared with that of existing nuclei segmentation methods on the CoNIC data set and the corresponding results are reported in Table V. From the results provided in Table V, it can be easily observed that, in case of CoNIC data set, the proposed Ostrich model outperforms existing nuclei segmentation approaches with respect all the evaluation indices. The high precision and low recall values of Stardist ensure the fact that it is confident about a few positive instances it predicts, but misses a substantial number of true positive instances. The segmentation performance of the proposed Ostrich model is also validated through a qualitative comparison presented in Fig. 8. The qualitative comparison through zoomed-in regions of the segmentation maps makes it clear that the proposed Ostrich model captures the nuclei structures better than most of the existing approaches. Finally, analyzing the p-values

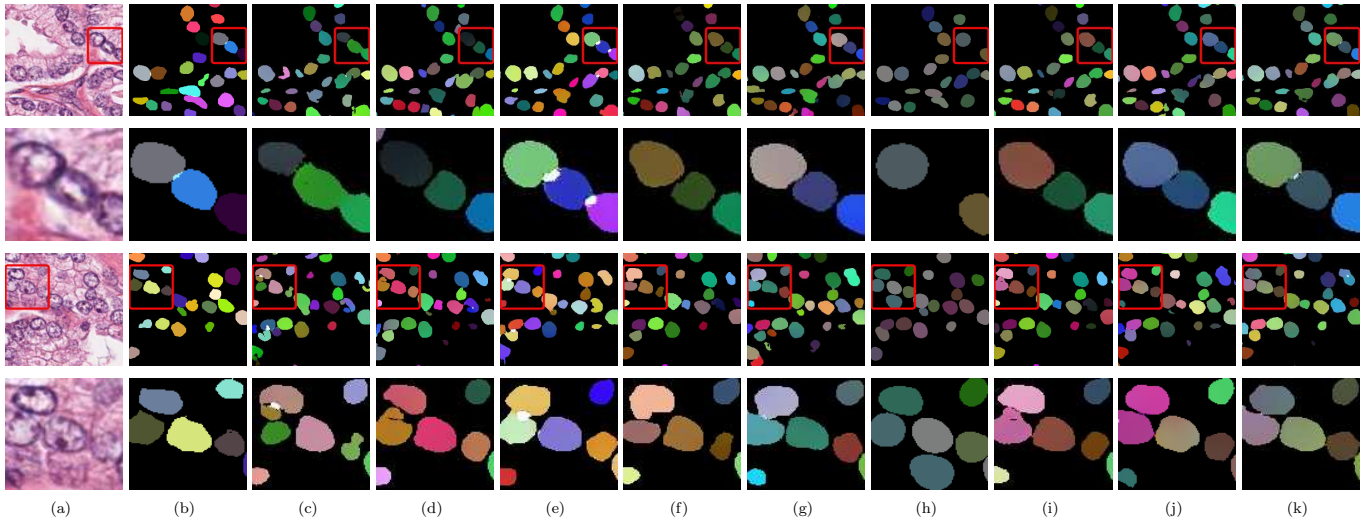


Fig. 7. (a) Original images of TCGA data, (b) ground-truth segmentation map; and segmentation maps obtained using existing nuclei segmentation methods: (c) U-Net (2015), (d) Mask-R-CNN (2017), (e) U-Net++ (2018), (f) HoVer-Net (2019), (g) MoNS (2020), (h) Stardist (2022), (i) Swin-MIL (2022), (j) BoNuS (2024) and (k) Ostrich. Row 1 and row 3 present two marked-up images from TCGA data, and row 2 and row 4 present the zoomed-in regions corresponding to the marked-up image patches in row 1 and row 3, respectively.

reported in Table VI, it can be noted that the proposed Ostrich model performs significantly better in 34 out of 36 cases, better but not significantly in 2 cases, with respect paired- t test. From the p-values reported in Table VI, it can also be observed that, irrespective of paired- t and Wilcoxon signed-rank tests, the proposed Ostrich model performs significantly better in 34 out of 36 cases, better but not significantly in just 2 cases. In Table VI, the p-values less than or equal to 9.99E-99 are reported as 9.99E-99.

TABLE V
QUANTITATIVE PERFORMANCE ANALYSIS IN NUCLEI SEGMENTATION ON CONIC DATA SET: STATE-OF-THE-ART MODELS VS OSTRICH

Methods	Dice	Jaccard	Precision	Recall
Ostrich	0.741107	0.591310	0.769381	0.793093
U-Net (2015)	0.715636	0.561178	0.704462	0.681140
Mask-R-CNN (2017)	0.717821	0.562671	0.725431	0.706849
U-Net++ (2018)	0.721316	0.568022	0.721591	0.706789
HoVer-Net (2019)	0.740318	0.590560	0.747550	0.698034
MoNS (2020)	0.722989	0.568692	0.722632	0.733005
Stardist (2022)	0.374534	0.240549	0.716413	0.275528
Swin-MIL (2022)	0.715991	0.560825	0.764054	0.682995
BoNuS (2024)	0.724678	0.571128	0.753906	0.768233

The quantitative results reported in Table I and Table V, and the qualitative analyses presented in Fig. 7 and Fig. 8 ensure the fact that the proposed Ostrich model outperforms the state-of-the-art nuclei segmentation approaches in almost all the cases. The proposed model performs consistently well in different types of nuclei segmentation tasks due to the following facts: (a) it employs I2I translation paradigm, which is invariant to different target domain representations, and (b) incorporation of an additional embedding space helps the proposed model to balance information disparity between two asymmetric image domains.

IV. CONCLUSION

Nuclei segmentation is one of the fundamental and critical steps in histological image analysis as it aids in subsequent

TABLE VI
STATISTICAL SIGNIFICANCE ANALYSIS OF DIFFERENT ALGORITHMS WITH RESPECT TO PAIRED- t (ONE-TAILED) AND WILCOXON SIGNED RANK (ONE-TAILED) TESTS ON CONIC DATA

Methods	Test	Dice	Jaccard	Precision	Recall
U-Net (2015)	Paired- t	1.21E-85	1.27E-86	9.99E-99	9.99E-99
Mask-R-CNN (2017)		9.99E-99	1.11E-99	9.99E-99	9.99E-99
U-Net++ (2018)		1.02E-63	2.46E-87	9.99E-99	9.99E-99
HoVer-Net (2019)		<i>8.81E-02</i>	<i>1.44E-01</i>	4.57E-98	9.99E-99
MoNS (2020)		9.99E-99	9.99E-99	9.99E-99	9.99E-99
Stardist (2022)		9.99E-99	1.11E-99	1.24E-82	9.99E-99
Swin-MIL (2022)		9.99E-99	9.99E-99	5.75E-20	9.99E-99
BoNuS (2024)		4.28E-78	1.12E-93	9.99E-99	9.99E-99
U-Net (2015)	Wilcoxon	1.17E-71	2.67E-71	9.99E-99	9.99E-99
Mask-R-CNN (2017)		9.99E-99	9.99E-99	9.99E-99	9.99E-99
U-Net++ (2018)		9.99E-99	9.99E-99	9.99E-99	9.99E-99
HoVer-Net (2019)		<i>1.93E-01</i>	<i>2.56E-01</i>	9.99E-99	9.99E-99
MoNS (2020)		9.99E-99	9.99E-99	9.99E-99	9.99E-99
Stardist (2022)		9.99E-99	1.11E-99	1.08E-83	9.99E-99
Swin-MIL (2022)		9.99E-99	9.99E-99	2.37E-31	9.99E-99
BoNuS (2024)		9.99E-99	9.99E-99	9.99E-99	9.99E-99

analysis of tissue specimens to estimate tumor cellularity, which is very crucial in the diagnosis and prognosis of cancer patients. In this respect, the main contributions of the current study are listed as follows:

- development of a deep generative model for segmenting nuclei regions from histological images, which considers an embedding space to handle information-imbalance between two image domains;
- development of an invertible generator, which achieves asymmetric I2I translation with lower network complexity;
- introduction of a regularization term to perturb image generation towards the accurate direction at the initial stage of training; and
- demonstrating the effectiveness of the proposed model, along with a comparison with existing algorithms, on publicly available H&E stained histology image data sets.

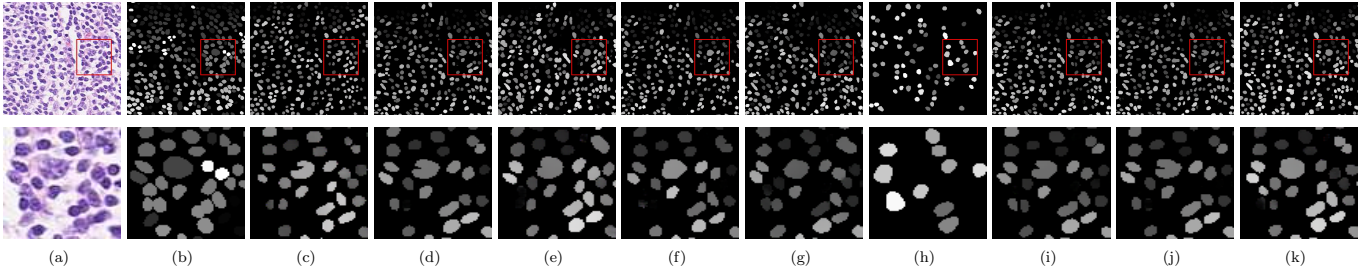


Fig. 8. (a) Original images of CoNIC data, (b) ground-truth segmentation map; and segmentation maps obtained using different nuclei segmentation methods: (c) U-Net (2015), (d) Mask-RCNN (2017), (e) U-Net++ (2018), (f) HoVer-Net (2019), (g) MoNS (2020), (h) Stardist (2022), (i) Swin-MIL (2022), (j) BoNuS (2024) and (k) Ostrich. Top row presents a marked-up images from CoNIC data, and bottom row presents the zoomed-in region from the marked-up patches.

The proposed model utilizes I2I translation paradigm, which enhances the applicability of the model in different types of nuclei segmentation tasks. From the quantitative and qualitative analysis presented in this paper, it is evident that the proposed model performs consistently well in both binary semantic segmentation and instance segmentation tasks with different types of target domain image representations. The proposed model does not consider any prior information about the shape of nuclei structures, which helps the model to capture heterogeneous nuclei shapes from tissue images belonging to different organs.

as follows:

APPENDIX

This section presents the derivation of the dual formulation corresponding to the primal form presented in (1):

$$\inf_{\pi \in \Pi(\mu, \nu, \eta)} \int_{\mathcal{X} \times \mathcal{Y} \times \mathcal{Z}} \mathcal{C}(x, y, z; G_\theta, F_\phi, E_\omega) d\pi(x, y, z) \quad (32)$$

where the transportation cost $\mathcal{C}(x, y, z; G_\theta, F_\phi, E_\omega)$ is defined in (4). So, (32) can be reformulated as follows:

$$\inf_{\pi \in \Pi(\mu, \nu, \eta)} \int_{\mathcal{X} \times \mathcal{Y} \times \mathcal{Z}} \hat{\mathcal{C}}(x, y, z) d\pi(x, y, z) + \lambda_1 l_{ssim}(F_\phi) \quad (33)$$

where $l_{ssim}(F_\phi)$ is defined in (3) and

$$\hat{\mathcal{C}}(x, y, z) = \|x - G_\theta(y, z)\| + \|F_\phi(x) - y\| + \|E_\omega(x) - z\|. \quad (34)$$

To compute the dual formulation of the above primal, let

$$K(G_\theta, F_\phi, E_\omega) = \min_{\pi \in \Pi(\mu, \nu, \eta)} \int_{\mathcal{X} \times \mathcal{Y} \times \mathcal{Z}} \hat{\mathcal{C}}(x, y, z) d\pi(x, y, z). \quad (35)$$

Let π^* be the optimal joint measure, that is, $\pi^* = \arg \min_{\pi \in \Pi(\mu, \nu, \eta)} \pi$, then (35) can be rewritten as follows:

$$K(G_\theta, F_\phi, E_\omega) = \int_{\mathcal{X} \times \mathcal{Y} \times \mathcal{Z}} \hat{\mathcal{C}}(x, y, z) d\pi^*(x, y, z). \quad (36)$$

Using (34), Kantorovich duality theorem [23] and c-transforms of Kantorovich potentials φ , ψ , and ξ , (36) can be rewritten

$$\begin{aligned} K(G_\theta, F_\phi, E_\omega) &= \int_{\mathcal{X} \times \mathcal{Y} \times \mathcal{Z}} \{ \|x - G_\theta(y, z)\| + \|F_\phi(x) - y\| \\ &\quad + \|E_\omega(x) - z\| \} d\pi^*(x, y, z) \\ &= \frac{1}{3} \{ \max_{\varphi} [\int_{\mathcal{X}} \varphi(x) d\mu(x) + \int_{\mathcal{Y} \times \mathcal{Z}} \inf_x [\|x - G_\theta(y, z)\| \\ &\quad + \|F_\phi(x) - y\| + \|E_\omega(x) - z\| - \varphi(x)] d(\nu \times \eta)(y, z)] \\ &\quad + \max_{\psi} [\int_{\mathcal{Y}} \psi(y) d\nu(y) + \int_{\mathcal{X}} \inf_y [\|x - G_\theta(y, z)\| + \|F_\phi(x) - y\| \\ &\quad + \|E_\omega(x) - z\| - \psi(y)] d\mu(x)] \\ &\quad + \max_{\xi} [\int_{\mathcal{Z}} \xi(z) d\eta(z) + \int_{\mathcal{X}} \inf_z [\|x - G_\theta(y, z)\| + \|F_\phi(x) - y\| \\ &\quad + \|E_\omega(x) - z\| - \xi(z)] d\mu(x)] \}. \end{aligned} \quad (37)$$

It can be noted from the optimization perspective that $\|E_\omega(x) - z\|$ and $\|F_\phi(x) - y\|$ are not dependant on \mathcal{Y} and \mathcal{Z} space, respectively. Now, instead of finding \inf_x , $x = G_\theta(y, z) = G_{\theta y}(z) = G_{\theta^z}(y)$ is chosen. Again, instead of finding \inf_y and \inf_z , if $y = F_\phi(x)$, and $z = E_\omega(x)$, respectively, are chosen, then an upper bound of $K(G_\theta, F_\phi, E_\omega)$ can

be obtained from (37) as follows:

$$\begin{aligned}
& K(G_\theta, F_\phi, E_\omega) \\
& \leq \frac{1}{3} \left\{ \max_{\varphi} \left[\int_{\mathcal{X}} \varphi(x) d\mu(x) - \int_{\mathcal{Y} \times \mathcal{Z}} \varphi(G_\theta(y, z)) d(\nu \times \eta)(y, z) \right] \right. \\
& \quad + \max_{\psi} \left[\int_{\mathcal{Y}} \psi(y) d\nu(y) - \int_{\mathcal{X}} \psi(F_\phi(x)) d\mu(x) \right] \\
& \quad + \max_{\xi} \left[\int_{\mathcal{Z}} \xi(z) d\eta(z) - \int_{\mathcal{X}} \xi(E_\omega(x)) d\mu(x) \right] \\
& \quad + \int_{\mathcal{Y} \times \mathcal{Z}} [\|y - F_\phi(G_\theta(y, z))\| + \|z - E_\omega(G_\theta(y, z))\|] \\
& \quad \quad d(\nu \times \eta)(y, z) \\
& \quad + \int_{\mathcal{X}} [\|x - G_\theta(F_\phi(x), z)\| + \|x - G_\theta(y, E_\omega(x))\|] d\mu(x) \left. \right\} \\
& \Rightarrow K(G_\theta, F_\phi, E_\omega) \leq \frac{1}{3} \{ l_{GAN}(G_\theta, F_\phi, E_\omega; \varphi, \psi, \xi) \\
& \quad + l_{cycle}(G_\theta, F_\phi, E_\omega) \} \quad (38)
\end{aligned}$$

where $l_{GAN}(G_\theta, F_\phi, E_\omega; \varphi, \psi, \xi)$ and $l_{cycle}(G_\theta, F_\phi, E_\omega)$ are defined in (7) and (8), respectively. Again, using 1-Lipschitz continuity of Kantorovich potentials φ , ψ , and ξ , the following relation can be obtained:

$$\begin{aligned}
& \varphi(x) - \varphi(G_\theta(y, z)) \leq \|x - G_\theta(y, z)\| \leq \|x - G_\theta(y, z)\| \\
& \quad + \|F_\phi(x) - y\| + \|E_\omega(x) - z\| \\
& \Rightarrow -\varphi(G_\theta(y, z)) \leq \|x - G_\theta(y, z)\| - \varphi(x) \\
& \leq \|x - G_\theta(y, z)\| + \|F_\phi(x) - y\| + \|E_\omega(x) - z\| - \varphi(x). \quad (39)
\end{aligned}$$

Similarly, the following relations can be obtained:

$$\begin{aligned}
& -\psi(F_\phi(x)) \leq \|F_\phi(x) - y\| - \psi(y) \\
& \leq \|x - G_\theta(y, z)\| + \|F_\phi(x) - y\| + \|E_\omega(x) - z\| - \psi(y) \quad (40)
\end{aligned}$$

$$\begin{aligned}
& \text{and} \quad -\xi(E_\omega(x)) \leq \|E_\omega(x) - z\| - \xi(z) \\
& \leq \|x - G_\theta(y, z)\| + \|F_\phi(x) - y\| + \|E_\omega(x) - z\| - \xi(z) \quad (41)
\end{aligned}$$

The inequalities (39)-(41) lead to the following lower bound:

$$K(G_\theta, F_\phi, E_\omega) \geq \frac{1}{3} l_{GAN}(G_\theta, F_\phi, E_\omega; \varphi, \psi, \xi). \quad (42)$$

It is evident from (38) and (42) that if $l_{cycle}(G_\theta, F_\phi, E_\omega)$ vanishes, then the following relation can be obtained:

$$K(G_\theta, F_\phi, E_\omega) = \frac{1}{3} l_{GAN}(G_\theta, F_\phi, E_\omega; \varphi, \psi, \xi). \quad (43)$$

From the optimization perspective, the normalizing constant $\frac{1}{3}$ in (43) can be ignored.

REFERENCES

- [1] J. G. Elmore et al., "Diagnostic Concordance Among Pathologists Interpreting Breast Biopsy Specimens," *The Journal of the American Medical Association*, vol. 313, no. 11, pp. 1122–1132, 2015.
- [2] P. Filipczuk et al., "Computer-Aided Breast Cancer Diagnosis Based on the Analysis of Cytological Images of Fine Needle Biopsies," *IEEE Transactions on Medical Imaging*, vol. 32, no. 12, pp. 2169–2178, 2013.
- [3] M. Veta et al., "Automatic Nuclei Segmentation in H&E Stained Breast Cancer Histopathology Images," *Plos One*, vol. 8, no. 7, p. e70221, 2013.
- [4] S. Ali and A. Madabhushi, "An Integrated Region-, Boundary-, Shape-Based Active Contour for Multiple Object Overlap Resolution in Histological Imagery," *IEEE Transactions on Medical Imaging*, vol. 31, no. 7, pp. 1448–1460, 2012.
- [5] J. T. Kwak et al., "Nucleus Detection Using Gradient Orientation Information and Linear Least Squares Regression," in *Proceedings of Medical Imaging: Digital Pathology*, vol. 9420, 2015, pp. 152–159.
- [6] C.-S. Chang et al., "Cell Segmentation Algorithm Using Double Thresholding with Morphology-Based Techniques," in *Proceedings of IEEE International Conference on Consumer Electronics, Taiwan*, 2018, pp. 1–5.
- [7] J. Song, L. Xiao, and Z. Lian, "Contour-Seed Pairs Learning-Based Framework for Simultaneously Detecting and Segmenting Various Overlapping Cells/Nuclei in Microscopy Images," *IEEE Transactions on Image Processing*, vol. 27, no. 12, pp. 5759–5774, 2018.
- [8] J. Song et al., "Multi-Layer Boosting Sparse Convolutional Model for Generalized Nuclear Segmentation from Histopathology Images," *Knowledge-Based Systems*, vol. 176, pp. 40–53, 2019.
- [9] O. R. et al., "U-Net: Convolutional Networks for Biomedical Image Segmentation," in *Proceedings of Medical Image Computing and Computer-Assisted Intervention*, 2015, pp. 234–241.
- [10] Z. Zhou et al., "UNet++: A Nested U-Net Architecture for Medical Image Segmentation," in *Proceedings of Deep Learning in Medical Image Analysis and Multimodal Learning for Clinical Decision Support*, 2018, pp. 3–11.
- [11] S. E. A. Raza et al., "Micro-Net: A Unified Model for Segmentation of Various Objects in Microscopy Images," *Medical Image Analysis*, vol. 52, pp. 160–173, 2019.
- [12] Preity, A. K. Bhandari and S. Shah Nawazuddin, "Soft Attention Mechanism Based Network to Extract Blood Vessels From Retinal Image Modality," *IEEE Transactions on Artificial Intelligence*, vol. 5, no. 7, pp. 3408–3418, 2024.
- [13] K. He et al., "Mask R-CNN," in *Proceedings of IEEE International Conference on Computer Vision*, 2017, pp. 2961–2969.
- [14] S. Graham et al., "Hover-Net: Simultaneous Segmentation and Classification of Nuclei in Multi-Tissue Histology Images," *Medical Image Analysis*, vol. 58, p. 101563, 2019.
- [15] M. Weigert and U. Schmidt, "Nuclei Instance Segmentation and Classification in Histopathology Images with Stardist," in *Proceedings of IEEE International Symposium on Biomedical Imaging Challenges*, 2022, pp. 1–4.
- [16] Lijin P. et al., "Dual Encoder-Decoder Shifted Window-Based Transformer Network for Polyp Segmentation With Self-Learning Approach," *IEEE Transactions on Artificial Intelligence*, vol. 5, no. 7, pp. 3456–3469, 2024.
- [17] Z. Qian et al., "Transformer Based Multiple Instance Learning for Weakly Supervised Histopathology Image Segmentation," in *Proceedings of Medical Image Computing and Computer Assisted Intervention*, 2022, pp. 160–170.
- [18] Y. Lin et al., "BoNuS: Boundary Mining for Nuclei Segmentation with Partial Point Labels," *IEEE Transactions on Medical Imaging*, vol. 43, no. 6, pp. 2137–2147, 2024.
- [19] J. -Y. Zhu et al., "Unpaired Image-to-Image Translation Using Cycle-Consistent Adversarial Networks," in *Proceedings of IEEE International Conference on Computer Vision*, 2017, pp. 2242–2251.
- [20] F. Mahmood et al., "Deep Adversarial Training for Multi-Organ Nuclei Segmentation in Histopathology Images," *IEEE Transactions on Medical Imaging*, vol. 39, no. 11, pp. 3257–3267, 2020.
- [21] S. Liu et al., "Unpaired Stain Transfer Using Pathology-Consistent Constrained Generative Adversarial Networks," *IEEE Transactions on Medical Imaging*, vol. 40, no. 8, pp. 1977–1989, 2021.
- [22] T. Kwon and J. C. Ye, "Cycle-Free CycleGAN Using Invertible Generator for Unsupervised Low-Dose CT Denoising," *IEEE Transactions on Computational Imaging*, vol. 7, pp. 1354–1368, 2021.
- [23] C. Villani, *Optimal Transport: Old and New*, ser. Grundlehren Der Mathematischen Wissenschaften. Springer Berlin Heidelberg, 2008.
- [24] W. Zhou et al., "Image Quality Assessment: From Error Visibility to Structural Similarity," *IEEE Transactions on Image Processing*, vol. 13, no. 4, pp. 600–612, 2004.

- [25] N. Otsu, "A Threshold Selection Method from Gray-Level Histograms," *IEEE Transactions on Systems, Man, and Cybernetics*, vol. 9, no. 1, pp. 62–66, 1979.
- [26] G. Peyré and M. Cuturi, *Computational Optimal Transport: With Applications to Data Science*, ser. Foundations and Trends in Machine Learning. Now Publishers, 2019.
- [27] D. L. Cohn, *Measure Theory*, ser. Birkhäuser Advanced Texts Basler Lehrbücher. Springer New York, 2013.
- [28] L. Dinh and J. S. -Dickstein and S. Bengio, "Density Estimation Using Real NVP," in *Proceedings of International Conference on Learning Representations*, 2017.
- [29] J. M. Tomczak, "General Invertible Transformations for Flow-based Generative Modeling," in *Proceedings of International Conference on Machine Learning Workshop on Invertible Neural Networks, Normalizing Flows, and Explicit Likelihood Models*, 2021.
- [30] N. Kumar et al., "A Dataset and a Technique for Generalized Nuclear Segmentation for Computational Pathology," *IEEE Transactions on Medical Imaging*, vol. 36, no. 7, pp. 1550–1560, 2017.
- [31] S. Graham et al., "Conic: Colon nuclei identification and counting challenge 2022," *arXiv preprint arXiv:2111.14485*, 2021.